Optics Communications 569 (2024) 130831

Contents lists available at ScienceDirect

Optics Communications

journal homepage: www.elsevier.com/locate/optcom

Generation of second harmonic at wide conversion band in GRIN multimode fibers

Maxime Jonard [a], Yago Arosa [a,b,*], Alessandro Tonello [a], Tigran Mansuryan [a], Maggy Colas [c], Julie Cornette [c], Jean-René Duclère [c], Claire Lefort [a], Vincent Couderc [a]

[a] Université de Limoges, XLIM UMR CNRS 7252, 123 Avenue A. Thomas, 87060, Limoges, France
[b] Dpto. de Física Aplicada, Univ. de Santiago de Compostela, 15705, Santiago de Compostela, Spain
[c] IRCER, UMR CNRS 7315, Université de Limoges, France

ARTICLE INFO

Keywords:
Second harmonic generation
Non-linear optics
Optical fibers
Frequency conversion

ABSTRACT

Optical poling of multimode graded-index fibers (GRIN) has emerged as a promising technique for creating periodic inscriptions of the second-order nonlinear optical susceptibility $\chi^{(2)}$, enabling the generation of a second harmonic in silica fibers. In this work, we investigate the generation of multiple spectral peaks using a continuous broadband source in the infrared domain, generated in the same fiber by a femtosecond laser with a central wavelength different from the one used for the poling process. Building upon theoretical foundations, this work contributes at explaining how second and third-order nonlinear processes participate to the broad generation of the second harmonic in GRIN fibers.

1. Introduction

The concept of frequency conversion, with a particular focus on its application in optics, has garnered significant attention, especially within the realms of bio-imaging and microscopy, as well as related fields [1–3]. Fluorescence microscopy is one remarkable example that requires coherent light sources that can be tuned over the visible range [4], but unfortunately, there are not so many sources with these characteristics. Multiple techniques serve the purpose of creating these sources like spectral combs [5], modulated supercontinuum lasers [6], or (more recently) by means of second harmonic generation (SHG) in quadratic nonlinear media [7].

Since the pioneering work of Franken et al., who reported SHG using a ruby laser and a quartz crystal [8], SHG has become a hot topic. The second harmonic generation (SHG) phenomenon relies on a specific non-centrosymmetric structural arrangement in the crystal lattice. This arrangement causes the nonlinear susceptibility $\chi^{(2)}$ to lack independent irreducible tensor components, preventing centrosymmetric structures, such as silica, from displaying the SHG effect [9]. However, in 1986, Österberg and Margulis [10] discovered optical poling in single-mode fibers, resulting in SHG by breaking the centrosymmetry in the fiber core.

Subsequently, Stolen et al. [11] proposed a model where the interaction between a fundamental frequency (FF) pump and a second harmonic (SH) seed generates periodic DC polarization via the third-order nonlinear optical susceptibility $\chi^{(3)}$, enabling quasi-phase matching (QPM) between the two waves. This process can be attributed to electron charge motions that cause electric quadrupole and magnetic dipole moments [12,13]. Initially, SHG primarily occurred in the fundamental mode of the fiber, although a slight spatial refractive index change favoured emission in the LP_{11} mode [14]. The limitation of unconventional SHG in fiber has been attributed to competition with the Raman effect in single-mode optical fiber and the generation of geometric parametric instabilities (GPI) in multimode fibers [15,16]. Recently, Gemechu et al. demonstrated improved SH conversion efficiency through cascading in separately poled fiber segments, achieving an average power efficiency of 4.7% [17].

In 2017, Ceoldo et al. and Eftekhar et al. independently demonstrated SHG in multimode graded index (GRIN) fibers. Despite multimode propagation, they noted that the self-cleaning process, enabled by the high peak power of the fundamental pump wave, influenced the polarization process and led to self-organized SHG in the fundamental mode LP_{01}. SH efficiency was significantly enhanced, reaching over 6.5% even without prior seeding [18,19].

Beyond SHG from the pump fundamental beam, Ceoldo et al. demonstrated the formation of an unevenly spaced spectral peak set

* Corresponding author. Dpto. de Física Aplicada, Univ. de Santiago de Compostela, 15705, Santiago de Compostela, Spain.
E-mail address: yago.arosa.lobato@usc.es (Y. Arosa).

https://doi.org/10.1016/j.optcom.2024.130831
Received 22 March 2024; Received in revised form 26 June 2024; Accepted 28 June 2024
Available online 29 June 2024

around the SH wavelength. Sharp secondary peaks were observed near 532 nm, originating from the SHG of a broadband pump at 1064 nm. This led to a combination of quadratic and cubic nonlinear effects. These experiments employed sub-nanosecond pulses, minimizing the impact of intermodal time delays and ensuring high conversion efficiency.

Building upon the aforementioned discoveries, this study aims to broaden our understanding of SHG in multimode fibers by exploring the generation of tunable spectral peaks across the visible spectrum. We employed femtosecond lasers in optically poled fibers, specifically probing the poled fiber with a laser source centered at 1030 nm, a wavelength distinct from the one used in the poling process (1064 nm). This source undergoes broadening along the fiber, establishing a framework in which $\chi^{(2)}$ and $\chi^{(3)}$ processes cascade, akin to previous investigations [20]. While the theoretical foundation for this phenomenon has been previously explored in Ref. [18], the explanation for the observed harmonic peaks has only been partially addressed.

In our work, we observe a discrepancy in the peak positions at the fiber output as we deviate from the central wavelength around the SH wavelength. Additionally, an unsatisfactory explanation is found concerning the positions of certain low-power spectral lines that do not align with the QPM condition. These distinctive spectral features result from the coexistence of multiple longitudinal gratings in optically poled GRIN fibers obtained by the beating among multiple transverse modes at fundamental and SH wavelengths. The inscription of such a complex nonlinear structure, which varies along the transverse and longitudinal coordinates may also incorporate a path-average component of the $\chi^{(2)}$.

2. Experiment and data

Our experimental set-up is illustrated in Fig. 1. The multimode GRIN fiber was purchased from Alcatel (50/125 μm) with a numerical aperture of 0.2. The fiber was previously poled with a microchip laser at 1064 nm following a standard technique [16].

The fiber length was 2 m. The chemical composition of the fiber core (expressed in terms of mass fraction (wt%)) was determined using a scanning electron microscope (SEM). The measured Si, Ge and O contents at the center of the fiber are respectively 45 wt%, 15 wt% and 40 wt%, showing in addition a smooth parabolic profile inside the core. This information was used to calculate the dispersion curves of the lowest order modes of the fiber.

For broadband SHG, we used a femtosecond laser pump with a central wavelength at 1030 nm, bandwidth of 5 nm and repetition rate of 300 kHz. The chirp-free pulse duration was 250 fs, but pulses could be stretched up to 3 ps by a system of gratings. The differentiating factor of this experiment is the use of an ultrashort pump pulse with central wavelength and pulse duration slightly different from the laser we used for the poling process (transform limited pulses of 640 ps at 1064 nm).

To analyze the output beam at the fiber end, we used two optical spectrum analyzers (OSA) covering the near infrared domain (900–1300 nm) and the visible region (400–600 nm). The output spectra were measured at different pump peak powers, from 10 kW to 180 kW (see Fig. 2).

The spectrum at visible wavelengths presents a series of unevenly spaced peaks (Fig. 2a) as the pump power increases whereas the spectrum around the pump broadens in a more homogeneous manner under the effect of self-phase-modulation and soliton dynamics for wavelengths above 1.3 μm, (Fig. 2b). The majority of the peaks in the visible spectrum have narrow profiles (±3 nm). An in-depth examination of the results unveils that a series of high-amplitude peaks is interdigitated with a second series of peaks of lower amplitude, clearly seen in the two higher peak power curves (Fig. 2a). The efficiency is calculated by measuring the total output power carried by all the peaks in the visible range, and it is around 1% of the total energy input of the FF at maximum peak power (180 kW). This drastic downgrade in the efficiency compared to previous authors' achievements can be easily explained by the broadening nonlinear effects arising faster due to the temporal length of the pulse. Three key points can be underlined in such spectrum: i) none of the peaks are centered at the SH of the pump wavelength (515 nm), ii) the peak with the largest efficiency is centered at 532 nm (corresponding to the SH beam used for the poling process) and iii) peaks are not equally spaced. There are also other competing effects, for instance, the large peak at 480 nm is not originated by an equivalent quadratic nonlinearity but is likely generated by the Kerr effect in the frame of the GPI process [21].

In [18], a similar experimental setup was used, and an approximate collective approach was formulated to explain the phenomenon. In GRIN fiber, the collective beating of many modes results in the periodic modulation of refraction, forming a long period grating. This grating enables SHG of a broadband pump via QPM, interacting with the short beating between multimode FF and SH beams. To compute the short-scale period of the optical poling (Λ), in Ref. [18] it was considered the propagation constants at the fundamental wavelength ($\beta(\omega)$), and at the second harmonic ($\beta(2\omega)$) taking into consideration only the material

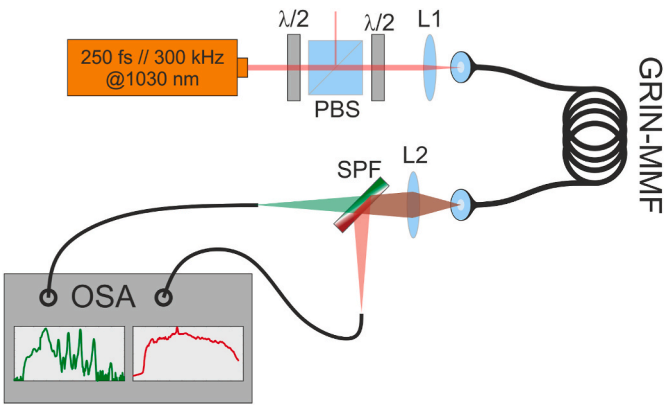

Fig. 1. Scheme of the experimental set-up. Femtosecond laser source, power regulation by two half waveplates and a polarizer beam splitter (PBS), injection (L1) and collection (L2) lenses, optical fiber (GRIN-MMF), short pass filter (SPF), and optical spectrum analyzer (OSA).

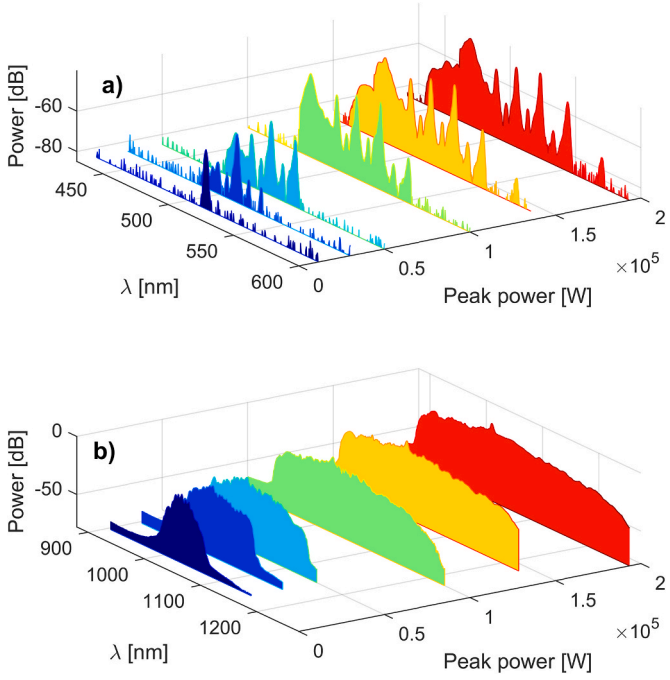

Fig. 2. (a) Spectra upon peak power in the visible domain close to the second harmonic of the pump. (b) Spectra upon peak power in the near infrared domain.

dispersion. The second long-scale period was considered to originate from the self-imaging of azimuthally symmetric beams (Λ_s). The beating periodicity and the self-imaging period ($\Lambda = 42.8\ \mu m, \Lambda_S = 590\ \mu m$) were in good agreement with the experimental values obtained by using multiphoton imaging ($\Lambda = 42\mu m, \Lambda_S = 543\ \mu m$) of a part of the poled core fiber, as shown also in Fig. 3.

The experimental analysis by SHG microscopy reported in Fig. 3 shows that the optical poling in a multimode fiber is considerably different from the standard picture of periodically poled material such as lithium niobate. First of all, the optical poling varies along the transverse and the longitudinal coordinates of the fiber. Under the effect of the self-imaging process and Kerr's nonlinearity, the beam at FF begins to self-clean [22] forcing part of the initial energy to converge towards lower order modes, while additional feeding of higher order modes is simultaneously observed [23]. Consequently, in the first part of the fiber, the coherent beating between the fundamental and SH multimode waves creates a complex nonlinear $\chi^{(2)}$ distribution composed of several interleaved gratings with a dominant periodicity (see Fig. 3a). During the reading process, when the FF beam is injected again in such section of poled fiber, the SHG takes place with modes propagating along an intricated distribution of a quadratic susceptibility $\chi^{(2)}(x,y,z)$, where we may also expect a nonzero path-average contribution.

As light propagates further along the multimode fiber, the beam undergoes a spatial self-cleaning process. This process concentrates more power on low-order modes, resulting in a central bell-shaped beam against a multimode background dominated by high-order modes |23]. The multimode beam at FF continues to interact with the second harmonic wave. A microscopic analysis reveals a more organized local inscription of the quadratic susceptibility at this stage. Although the low-power multimode background is minimized, its disappearance is not complete, contributing to a continuous component of the written nonlinearity. The appearance of the two main gratings can be explained by the dependency of the quadratic susceptibility to the transverse gradient of the FF beam shape [24] (Fig. 3b).

The phase mismatch between fundamental and second harmonic, $\Delta\beta(\omega) = \beta(2\omega) - 2\beta(\omega)$ being $\beta(\omega) = n_0(\omega)k_0(\omega)$. The propagation constat of each frequency, was evaluated by considering only the material dispersion neglecting the waveguide contribution and was limited to standard silica glass (overlooking small shifts due to the exact nature of the fiber glass). The QPM equation to observe SHG was then:

$$\Delta\beta(\omega) - \frac{2\pi}{\Lambda} - q\frac{2\pi}{\Lambda_s} = 0 \tag{1}$$

where q is any integer number determining the harmonic resonance order. We validated the predictions of (Eq. (1)), by comparing them with experimental results in multiphoton microscope (see Fig. 3). Both short and long-scale periods contribute to the QPM, with the long-scale period responsible for the uneven distribution of multiple peaks due to the material dispersion. A deeper look into the transverse profile, after applying neural network denoising, shows that $\chi^{(2)}$ is the highest in a circular shape (also seen as a tubular shape in the longitudinal cut) with a smaller central spot. The transversal distribution of the $\chi^{(2)}$ susceptibility could be attributed to the poling process involving many modes at the second harmonic. This circular shape overlays a homogenous baseline of $\chi^{(2)}$ in the core of the fiber, not seen in the cladding (Fig. 4).

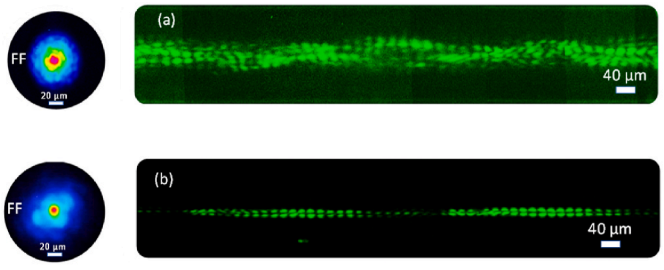

Fig. 3. $\chi^{(2)}$ inscription obtained by multiphoton imaging. (a) Image in the first part (0–1 m) of the fiber with an incomplete self-cleaning process; (b) $\chi^{(2)}$ nonlinearity distribution with a self-cleaned beam at FF showing the upper part of the main two periodic gratings. Insets (left): images of the output FF beam leading to the poling process.

The analysis of Ref. [18] was limited to the self-imaging period of symmetric beams. However, there exist other modal combinations to satisfy the QPM condition, especially for skew rays with a zig-zag trajectory twice as long as the self-imaging period Λ_s for azimuthally invariant modes. This intuitive reasoning underscores the necessity of employing modal analysis, as multiple additional pairs of propagation constants can potentially satisfy the phase matching condition.

3. Theoretical approach

In this work we aim at addressing the problem more fundamentally by considering the perfect phase matching condition using the exact propagation constants of each mode. To begin with, we consider the limit of weak conversion regime [25] between the second harmonic (SH) and fundamental frequency (FF) for the guided modes in GRIN fibers [26]. Both beams, SH and FF, can be expressed as the linear combination of modes:

$$E_\omega(x,y,z) = \sum_{k,n} a_{kn}(z)\cdot\Psi^{\omega}_{\mathrm{kn}}(x,y)\cdot e^{-j\beta^{kn}_{\omega}z} \tag{2}$$

$$E_{2\omega}(x,y,z) = \sum_{l,m} b_{lm}(z)\cdot\Psi^{2\omega}_{\mathrm{lm}}(x,y)\cdot e^{-j\beta^{lm}_{2\omega}z} \tag{3}$$

Where the electric fields $E_\omega(x,y,z)$ and $E_{2\omega}(x,y,z)$ are a function of their normalized eigenfunctions, $\Psi^{\omega}_{kn}(x,y)$, $\Psi^{2\omega}_{lm}(x,y)$ and their related propagation constants, β^{kn}_{ω} and $\beta^{lm}_{2\omega}$. The (complex) amplitude of each mode is described by functions $a_{kn}(z)$ for FF and $b_{lm}(z)$ for SH.

Expanding the equations for FF and SH in terms of guided modes allows us to compute the evolution of $b_{lm}(z)$ and the impact of the corresponding phase matching condition:

$$\frac{db_{lm}}{dz} = -j\cdot(a_{kn})^2\cdot f_{lmkn}(z)\cdot e^{-j\Delta\beta_{lmkn}z} \tag{4}$$

$$f_{lmkn}(z) = \iint \gamma(x,y,z)\cdot\Psi^{2\omega}_{lm}\cdot\left(\Psi^{\omega}_{kn}\right)^2 dxdy \tag{5}$$

$$\Delta\beta_{lmkn} = \left(2\beta^{kn}_{\omega} - \beta^{lm}_{2\omega}\right) \tag{6}$$

Where $\gamma(x,y,z)$ represents the inscribed non-linear coefficient during the poling process (proportional to $\chi^{(2)}$), $f_{lmkn}(z)$ is the coupling coefficient between two given modes l,m for the SH and k,n for FF, and $\Delta\beta_{lmkn}$ is the phase matching condition for these specific modes. We have simplified by considering only one mode in FF to avoid degeneracy (multiple mode convinations arising the same mismatch result); however, combinations involving two FF modes are also feasible, albeit with reduced coupling coefficients. We can make several reasonable assumptions: the FF is mainly carried by its fundamental mode, $\forall\,[k,n \neq 0,0]\ a_{kn} = 0$, and its power is almost constant over the propagation (undepleted pump), $a_{00}(z) \approx a_{00}$. Thus equation (2) can be simplified to:

$$E_\omega(x,y,z) = a_{00}\cdot\Psi^{\omega}_{00}(x,y)\cdot e^{-j\beta^{00}_{\omega}z} \tag{7}$$

Additionally, our total propagation length is far greater than the periodicity Λ of function $f_{lmkn}(z)$ measured by multiphoton microscopy ($\sim 42\ \mu m$). The nonlinear coupling function $f_{lmkn}(z)$ can be expanded in a Fourier series, where the first term will represent the path-average value $\overline{f_{lmkn}}$, and the second term will be responsible for the QPM with period Λ. In this work we will focus on the impact of the path-average component $\overline{f_{lmkn}}$ resembling the base line observed in Fig. 4 all over the core. These

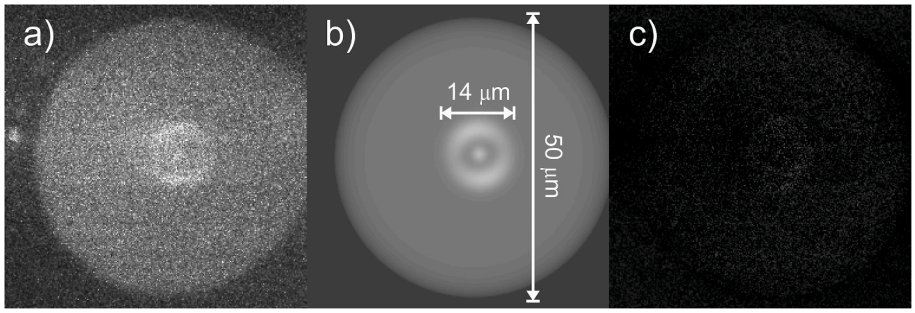

Fig. 4. Detection of the $\chi^{(2)}$ distribution in a poled fiber after self-cleaning. The image is obtained by multiphoton imaging in the core of the fiber; a) raw data, b) filtered data, c) residuals.

assumptions lead to the simplification of equations (4)–(6):

$$\frac{db_{lm}}{dz} = -j\cdot(a_{00})^2\cdot\overline{f_{lm}}\cdot e^{-j\Delta\beta_{lm00}z} \tag{8}$$

$$\overline{f_{lm}} = \overline{f_{lm00}} \tag{9}$$

$$\Delta\beta_{lm} = \Delta\beta_{lm00} = \left(2\beta_{\omega}^{00} - \beta_{2\omega}^{lm}\right) \tag{10}$$

We have simplified our notation to avoid the reference to the mode parameters of the FF as we consider only the fundamental mode. From equation (8), we derive the amplitude expression for a given mode under weak conversion, at a distance L:

$$b_{lm}(L) \simeq -j\cdot(a_{01})^2\cdot\overline{f_{lm}}\cdot e^{-j\Delta\beta_{lm}\frac{L}{2}}\cdot 2\frac{sin\left(\Delta\beta_{lm}\frac{L}{2}\right)}{\Delta\beta_{lm}} \tag{11}$$

So finally, the power carried by mode l, m at the SH could be written as:

$$|b_{lm}(L)|^2 \simeq |a_{00}|^4\cdot|\overline{f_{lm}}|^2\cdot 4\frac{sin^2\left(\frac{\Delta\beta_{lm}L}{2}\right)}{\Delta\beta_{lm}^2} \tag{12}$$

Using these modal amplitudes in equation (3), we calculate the power density of the SH at a given distance L. Additionally, these equations provide distinct insights: the coefficients f_{lm} delineate the spatial profile, while the phase matching condition defines the spectral distribution. The efficiency of SH conversion results from the combined action of these parameters, as described in equation (12). A similar approach was used by Hahn et al. [27] to explain frequency conversion in GaN and AlN slabs, observing an analogue set of preferred wavelengths for SHG in given slab waveguides.

4. Data analysis

These new phase matching combinations establish efficient wavelengths where SHG is locally maximized. As equation (6) approaches zero, it is possible to identify the wavelengths at which the SHG reaches its local maximum. In contrast with the approach in Ref. [18], in the present work we consider the presence of a constant or path-average quadratic susceptibility. To determine the new phase-matching curve, we calculate the propagation constants of desired FF wavelengths (near the pump due to spectral broadening) and identify the closest propagation constants for SH modes. Fig. 5 illustrates an example of this matching process: when the FF mode's propagation constant (yellow dashed) aligns with that of any SH mode (blue dotted) a maximum conversion efficiency is achieved ($\Delta\beta_{lm} = 0$). In this figure the orange and yellow lines represent the refractive indexes of the core (n_0) and cladding (n_1) at their respective wavelengths.

The propagation constants are function of the fiber geometry and material dispersion. In order to have a reliable dispersion curve we have

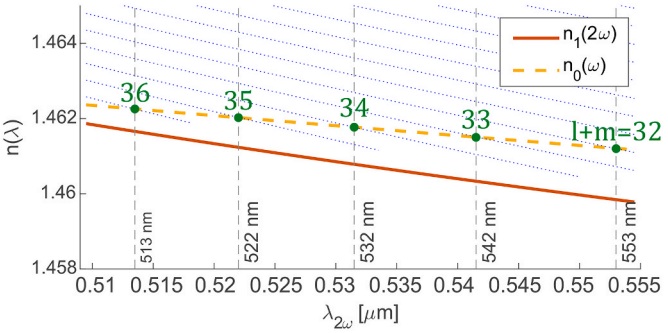

Fig. 5. Effective indices of the fiber modes in the visible spectrum. The solid orange curve is the cladding refractive index (n_1), the yellow dashed curve represents the effective index of mode Ψ_{00}^{ω} mode of the FF and the blue dotted curves are the effective indices of the other guided modes for SH. Vertical dashed lines and green dots highlight the best matching conditions and the mode level ($l + m$).

calculated the core and cladding dispersion curves using available data for SiO_2 and GeO_2 [28,29] and used a Dale-Gladstone relation [30]:

$$n_0^2 - 1 = \left(n_{Si}^2 - 1\right)x_{Si} + \left(n_{Ge}^2 - 1\right)x_{Ge} \tag{13}$$

Where n_i and x_i are the refractive index and molar fraction of each element. From this equation and based on the measured profile, we calculate the propagation constants as function of the wavelength. The best conversion efficiency is always chosen as the minimum distance from the propagation constant of Ψ_{00}^{ω}. The value of $\Delta\beta_{lm}$ and the QPM discussed in Ref. [18] are compared in Fig. 6

Both approaches yield similar peak values, with this work additionally predicting an extra set of lower-amplitude peaks. Furthermore, a shift in peak positions is observed as we move away from the SH of the

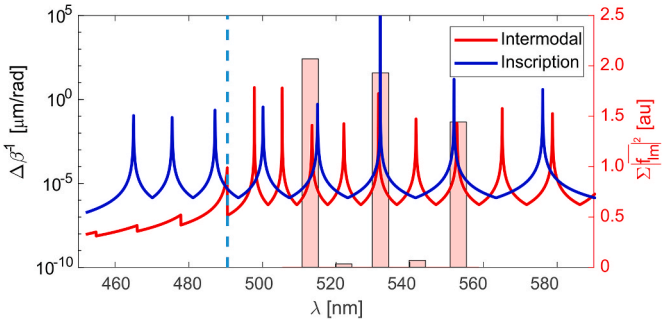

Fig. 6. QPM condition using the inscription periodicity match from (eq. (1)) (blue) and our intermodal phase-matching (red). The dashed line shows the limit for core guided modes in the SH. Red semi-transparent bars show the coupling coefficients (eq. (12)) for the 5 central wavelengths.

pump carrier wavelength, in our case 515 nm.

These similar results could be explained interpreting [18] as an approximation of the model proposed in the present work. In order to arrive there, we need to expand equation (6) for a GRIN fiber, where the propagation constant of a mode l, m at a given wavelength is described as follows:

$$\beta_{l,m} = \sqrt{n_0^2 k_0^2 - \frac{k_0 n_0}{R}\sqrt{2\Delta}[(2l+1)+(2m+1)]} \tag{14}$$

Where n_0 is the refractive index at the center of the core, k_0 is the free-space wavenumber at a given wavelength, R is the radius of the core and $\Delta = (n_0^2 - n_1^2)/2n_0^2$ is the relative refractive index difference with n_1 being the refractive index of the cladding. On top the explicit form of the propagation constants, we should apply two approximations: first, the modes being considered are far from the cutoff, low values of l, m, leading equation (14) into:

$$\beta_{l,m} \simeq n_0 k_0 \left(1 - \frac{1}{2}\frac{\sqrt{2\Delta}}{R n_0 k_0}[(2l+1)+(2m+1)]\right) \tag{15}$$

The second approximation assumes nearly achromatic relative refractive index difference, hence $\Delta(\omega) \simeq \Delta(2\omega)$. Using this second approximation, we can combine equations (15) and (6) to obtain the phase matching condition between two modes in a GRIN fiber. As expected in an optical fiber, eq. (15) shows that the propagation constant $\beta_{l,m}$ of the guided mode l,m is lower than the propagation constant of a plane wave in the center of the core $n_0 k_0$. This difference arises from a term depending on $\Delta, R,\ l,m$. The phase mismatch for SH generation in eq. (6) can be rewritten as follows:

$$\Delta\beta_{l,mk,n} \simeq 2\beta(\omega) - \beta(2\omega) - \frac{\sqrt{2\Delta}}{2R}[2[(2k+1)+(2n+1)] - [(2l+1)+(2m+1)]] \tag{16}$$

Where $\beta(\omega) = n_0(\omega)k_0(\omega)$. We can now compare this approach to the equation proposed by Ceoldo and coworkers in Ref. [18] shown in equation (1) to obtain QPM. We can easily identify how the first two terms of the right-hand side of eq. (16) are the phase mismatch $\Delta\beta(\omega)$ of SHG referred to two plane waves at ω and 2ω in a homogenous medium (core). The last term in eq. (16) is an integer multiple of the momentum provided by the period $2\Lambda_S$, where Λ_S is the self imaging period for radially symmetric beams $(2\pi/\Lambda_S = 2\sqrt{2\Delta}/R)$. Constant (h) arises from the possible combinations of (l,m,k, n), it is consistent with the parameter $q \in \mathbb{Z}$ found by Ceoldo et al…when h = 2q generalizing for any mode (not limited to radially invariant modes).

$$\Delta\beta_{l,mk,n} \simeq \Delta\beta(\omega) - h\frac{2\pi}{2\Lambda_s} \tag{17.a}$$

$$h = (l+m) - 2(k+n) - 1 \tag{17.b}$$

The major difference between equations (6) and (1) is then the momentum of the QPM of order 1 arising from the poling period Λ not considered in equation (6). Equation (1) demonstrates that in a medium with doubly periodic quadratic susceptibility, SHG can occur via QPM involving many pairs of modes at FF and SH. In contrast, equation (6) illustrates that in a multimode fiber, modal phase matched SHG can be achieved through selected pairs of guided modes even in a medium with longitudinally constant component of the quadratic nonlinearity. It is also worth noting that the approach shown here only considers guided modes, resulting in a lower wavelength limit when the cladding index at the SH is higher than the core index at the FF (dashed light blue line in Fig. 6).

In order to compare this multimodality arising from the intermodal SHG, Fig. 7 shows the spatial profile of the three most intense peaks

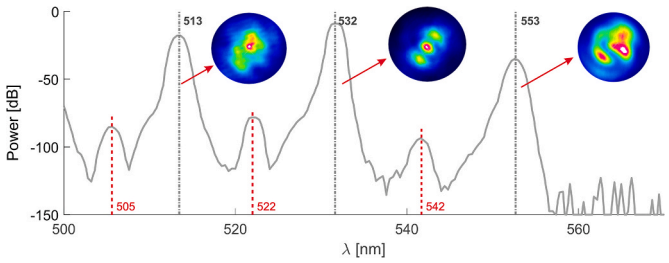

Fig. 7. Spatial profile of the three main peaks of the SH conversion (dot-dashed grey lines) and the lower set of peaks (dashed red lines).

(measured experimentally) proving their multimodal nature and how all of them are different in shape (different l, m involved). Here, coupling coefficients align with phase matching conditions, ensuring optimal conversion in modes with higher coupling coefficients. This alignment results in the observed interspersing of high (dashed grey) and lower (dashed red) peaks. These coefficients were calculated from equation (9) and adding all the squares for the degenerated modes, modes with the same propagation constant. As it is shown in Fig. 6 (bars), these coefficients show an alternating due to the symmetry properties of the modes involved in the conversion, manifesting as interdigitated higher $(l+m = 2p)$ and lower peaks $(l+m = 2p+1)$.

In Fig. 8, it is shown both the spectrum obtained with the 200 kW peak power of the pump (in order to observe maximum broadening) and the predicted peak positions considering both intermodal phase-matching and the coupling coefficients obtained by the propagation of each wave present in the experimental pump. As said before, we have considered that all the power $P_{exp}(\omega)$ at FF is carried by the fundamental mode, $P_{exp}(\omega) = |a_{00}(\omega)|^2$. Despite expectations of a more speckled beam due to modes near cutoff, the observed pattern cleaning could be attributed to linear mode coupling or cross-phase modulation (XPM) interactions with FF [31]. The presence of the low order modes can be also explained by the concurrent SHG conversion supported by the QPM of order 1.

Using both approaches, we can now properly predict not only the position of the peaks (almost a perfect match with the experimental data), but also the alternating between high and lower peaks. Although the last peak (478 nm) is predicted, it already corresponds to cladding modes, which should not be present due to the lack of overlap with the fundamental beam. We may speculate that this peak originates from the GPI in the fiber. Despite these accurate predictions, there are still some discrepancies, such as the asymmetric width of the higher peaks. This asymmetry could arise from mode coupling with the periodic grating created by the $\chi^{(2)}$ inscription (not considered in this study), cross-phase modulation interactions with the FF, or other processes not included in the present model

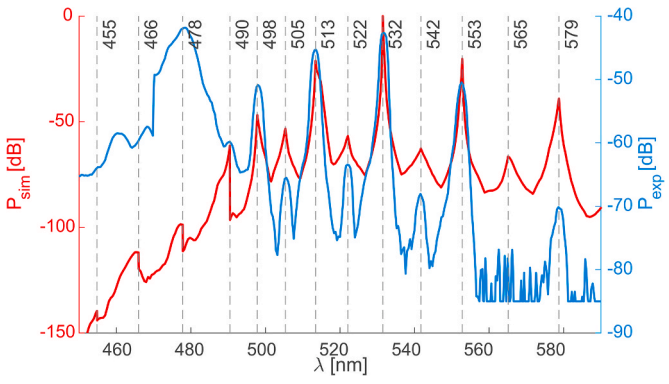

Fig. 8. Qualitative prediction (red) and experimental (blue) intensities for the SH spectrum. Dashed vertical lines indicates efficient peaks.

5. Conclusions

In this study, we expanded upon previous researches, investigating the creation of a set of spectral peaks over the visible spectrum in an optically poled multimode GRIN fiber with femtosecond lasers using a distinct fundamental pump wavelength from the one used for poling. Through systematic experimentation, we observed the emergence of several intense spectral peaks with sharp secondary peaks surrounding 532 nm, stemming from pump spectral broadening in the infrared range. This spectrum exhibited distinct traits: uneven wavelength distribution and two sets of varying intensity peaks. The introduction of intermodal phase matching improved our understanding of the appearance and intensity variations of these peaks.

Our findings deepen comprehension of nonlinear dynamics in optically poled multimode GRIN fibers and shed light on generating narrow spectral peaks with different pumping schemes and set wavelengths while maintaining short pulse duration, similar to that of the original source. The ability to generate specific invariant peaks regardless of the pump source used in the poling process opens new practical applications. Furthermore, the improved theoretical framework enhances our capacity to describe and predict this frequency conversion process and determine a priori the position of the characteristic peaks knowing the geometry and doping of the fiber. The unique spectral characteristics and versatility of these fiber-based sources offer promising prospects across multiple fields, including spectroscopy, biomedical imaging, and telecommunications.

Funding

Agence Nationale de la Recherche Labex SigmaLIM (10-LABX-0074-01). Y. Arosa. acknowledges a postdoctoral fellowship (ED481B-2021-027) from the Xunta de Galicia (Spain).

CRediT authorship contribution statement

Maxime Jonard: Writing – review & editing, Writing – original draft, Validation, Investigation, Conceptualization. **Yago Arosa:** Writing – original draft, Software, Formal analysis, Data curation, Conceptualization. **Alessandro Tonello:** Writing – review & editing, Validation, Supervision, Methodology. **Tigran Mansuryan:** Writing – review & editing, Validation. **Maggy Colas:** Writing – review & editing. **Julie Cornette:** Writing – review & editing. **Jean-René Duclère:** Writing – review & editing, Validation. **Claire Lefort:** Writing – review & editing, Validation, Data curation. **Vincent Couderc:** Writing – review & editing, Validation, Supervision, Resources, Formal analysis.

Declaration of competing interest

The authors declare that they have no known competing financial interests or personal relationships that could have appeared to influence the work reported in this paper.

Data availability

Data will be made available on request.

References

[1] K.A. Moldosanov, A.V. Postnikov, V.M. Lelevkin, N.J. Kairyev, Terahertz imaging technique for cancer diagnostics using frequency conversion by gold nano-objects, Ferroelectrics 509 (2017) 158–166.
[2] M. Baumgartl, M. Chemnitz, C. Jauregui, T. Meyer, B. Dietzek, J. Popp, J. Limpert, A. Tünnermann, All-fiber laser source for CARS microscopy based on fiber optical parametric frequency conversion, Opt. Express, OE 20 (2012) 4484–4493.
[3] H. Segawa, M. Okuno, P. Leproux, V. Couderc, T. Ozawa, H. Kano, Multimodal imaging of living cells with multiplex coherent anti-Stokes Raman scattering (CARS), third-order sum frequency generation (TSFG) and two-photon excitation fluorescence (TPEF) using a nanosecond white light laser source, Anal. Sci. 31 (2015) 299–305.
[4] J.W. Lichtman, J.-A. Conchello, Fluorescence microscopy, Nat. Methods 2 (2005) 910–919.
[5] T. Fortier, E. Baumann, 20 years of developments in optical frequency comb technology and applications, Commun. Phys. 2 (2019) 1–16.
[6] C. Poudel, C.F. Kaminski, Supercontinuum radiation in fluorescence microscopy and biomedical imaging applications, J. Opt. Soc. Am. B, JOSAB 36 (2019) A139–A153.
[7] I. Ricciardi, S. Mosca, M. Parisi, P. Maddaloni, L. Santamaria, P. De Natale, M. De Rosa, Frequency comb generation in quadratic nonlinear media, Phys. Rev. A 91 (2015) 063839.
[8] P.A. Franken, A.E. Hill, C.W. Peters, G. Weinreich, Generation of optical harmonics, Phys. Rev. Lett. 7 (1961) 118–119.
[9] D.A. Kleinman, Theory of second harmonic generation of light, Phys. Rev. 128 (1962) 1761–1775.
[10] U. Österberg, W. Margulis, Experimental studies on efficient frequency doubling in glass optical fibers, Opt. Lett. 12 (1987) 57–59.
[11] R.H. Stolen, H.W.K. Tom, Self-organized phase-matched harmonic generation in optical fibers, Opt. Lett., OL 12 (1987) 585–587.
[12] D.S. Bethune, Quadrupole second-harmonic generation for a focused beam of arbitrary transverse structure and polarization, Opt. Lett., OL 6 (1981) 287–289.
[13] F.P. Payne, Second-harmonic generation in single-mode optical fibres, Electron. Lett. 23 (1987) 1215–1216.
[14] U. Österberg, R.I. Lawconnell, L.A. Brambani, C.G. Askins, E.J. Friebele, Modal evolution of induced second-harmonic light in an optical fiber, Opt. Lett., OL 16 (1991) 132–134.
[15] V. Couderc, A. Tonello, C. Buy-Lesvigne, P. Leproux, L. Grossard, Unprecedented Raman cascading and four-wave mixing from second-harmonic generation in optical fiber, Opt. Lett., OL 35 (2010) 145–147.
[16] M. Jonard, M. Colas, Y. Leventoux, T. Mansuryan, J. Cornette, A. Tonello, S. Wabnitz, M. Zitelli, F. Mangini, M. Ferraro, Y. Sun, S. Février, J.-R. Duclère, V. Couderc, C. Lefort, Towards a new understanding of optical poling efficiency in multimode fibers, in: Nonlinear Optics and its Applications 2022, vol. 12143, SPIE, 2022, pp. 7–14.
[17] W.A. Gemechu, U. Minoni, D. Modotto, A. Tonello, V. Couderc, Efficient second-harmonic generation through cascaded optically poled fibers, Opt. Lett., OL 48 (2023) 668–671.
[18] D. Ceoldo, K. Krupa, A. Tonello, V. Couderc, D. Modotto, U. Minoni, G. Millot, S. Wabnitz, Second harmonic generation in multimode graded-index fibers: spatial beam cleaning and multiple harmonic sideband generation, Opt. Lett., OL 42 (2017) 971–974.
[19] M.A. Eftekhar, Z. Sanjabi-Eznaveh, J.E. Antonio-Lopez, F.W. Wise, D. N. Christodoulides, R. Amezcua-Correa, Instant and efficient second-harmonic generation and downconversion in unprepared graded-index multimode fibers, Opt. Lett., OL 42 (2017) 3478–3481.
[20] C.R. Phillips, C. Langrock, J.S. Pelc, M.M. Fejer, I. Hartl, M.E. Fermann, Supercontinuum generation in quasi-phasematched waveguides, Opt. Express, OE 19 (2011) 18754–18773.
[21] K. Krupa, A. Tonello, A. Barthélémy, V. Couderc, B.M. Shalaby, A. Bendahmane, G. Millot, S. Wabnitz, Observation of geometric parametric instability induced by the periodic spatial self-imaging of multimode waves, Phys. Rev. Lett. 116 (2016) 183901.
[22] Katarzyna Krupa, Alessandro Tonello, Alain Barthélémy, Couderc Vincent, Badr Mohamed Shalaby, Abdelkrim Bendahmane, Guy Millot, Stefan Wabnitz, Spatial beam self-cleaning in multimode fibres, Nat. Photonics 11 (4) (2016) 237–241.
[23] A. Fusaro, J. Garnier, K. Krupa, G. Millot, A. Picozzi, Dramatic acceleration of wave condensation mediated by disorder in multimode fibers, Phys. Rev. Lett. 122 (12) (2019) 123902.
[24] Vince Dominic, Jack Feinberg, High-resolution map of the dc electric field in second-harmonic-generating glass, J. Opt. Soc. Am. B 11 (1994).
[25] S. Ducci, L. Lanco, V. Berger, A. De Rossi, V. Ortiz, M. Calligaro, Continuous-wave second-harmonic generation in modal phase matched semiconductor waveguides, Appl. Phys. Lett. 84 (2004) 2974–2976.
[26] A.W. Snyder, J.D. Love, Optical Waveguide Theory, Chapman and Hall, London, 1983.
[27] D.N. Hahn, G.T. Kiehne, J.B. Ketterson, G.K.L. Wong, P. Kung, A. Saxler, M. Razeghi, Phase-matched optical second-harmonic generation in GaN and AlN slab waveguides, J. Appl. Phys. 85 (1999) 2497–2501.
[28] Y. Arosa, R. de la Fuente, Refractive index spectroscopy and material dispersion in fused silica glass, Opt. Lett., OL 45 (2020) 4268–4271.
[29] J.W. Fleming, Dispersion in GeO2–SiO2 glasses, Appl. Opt. AO 23 (1984) 4486–4493.
[30] W. Heller, Remarks on refractive index mixture rules, J. Phys. Chem. 69 (1965) 1123–1129.
[31] T. Mansuryan, Y. Arosa Lobato, A. Tonello, M. Ferraro, M. Zitelli, F. Mangini, Y. Sun, K. Krupa, B. Wetzel, S. Wabnitz, V. Couderc, Light-by-Light control enabled by incoherent beam superpositions in multimode fibres, in: 2023 Conference on Lasers and Electro-Optics Europe & European Quantum Electronics Conference (CLEO/Europe-EQEC), 2023, p. 1. Munich, Germany.